JGR Oceans

RESEARCH ARTICLE
10.1029/2022JC019291

Key Points:

- Eastern boundary current system captured in unprecedented detail using 22 months of near-continuous glider observations
- Large-scale freshening event in subpolar North Atlantic impacted Rockall Trough (RT) around 2017
- Interannual variability in poleward transport driven by subsurface temperature anomalies at the western flank of the RT

Correspondence to:
N. J. Fraser,
neil.fraser@sams.ac.uk

Citation:
Fraser, N. J., Cunningham, S. A., Drysdale, L. A., Inall, M. E., Johnson, C., Jones, S. C., et al. (2022). North Atlantic Current and European Slope Current circulation in the Rockall Trough observed using moorings and gliders. *Journal of Geophysical Research: Oceans*, *127*, e2022JC019291. https://doi.org/10.1029/2022JC019291

Received 15 SEP 2022
Accepted 24 NOV 2022

North Atlantic Current and European Slope Current Circulation in the Rockall Trough Observed Using Moorings and Gliders

Neil J. Fraser[1], Stuart A. Cunningham[1], Lewis A. Drysdale[1], Mark E. Inall[1], Clare Johnson[1], Sam C. Jones[1], Kristin Burmeister[1], Alan D. Fox[1], Estelle Dumont[1], Marie Porter[1], and N. Penny Holliday[2]

[1]The Scottish Association for Marine Science, Oban, UK, [2]National Oceanography Centre, Southampton, UK

Abstract The Rockall Trough (RT) accommodates the warmest and saltiest branch of the North Atlantic Current, which delivers water from the Gulf Stream into the marine environment around western Europe. In addition, the European Slope Current (ESC) carries warm water northward along the eastern boundary of the RT, and exchange between the ESC and the continental shelf is a dominant factor in determining the oceanographic conditions around the British Isles. However, the picture of the mean circulation and variability in the RT is still emerging, with a continuous observational campaign still in its relative infancy. The ESC, in particular, is poorly constrained by ship-based, mooring, and satellite observations. In this paper, we examine the RT circulation and volume transport using a temporally extended and spatially expanded observing network. Six years of continuous mooring occupation reveal that a large-amplitude, basin-scale freshening event, previously detected south of Iceland around 2015, impacted the RT around 2017. Geostrophic transport was greatly reduced during this period, driven by a concurrent subsurface temperature increase at the western boundary. The circulation regained strength during the latter part of the record. We gathered 110 glider transects over 22 months which capture the ESC velocity field in unprecedented detail. The data are sufficient to characterize both the mean state and the emergent seasonal variability of the ESC, and reveal the year-round presence of a southward countercurrent at depth. Variability in the strength and structure of this previously unstudied feature modulates net northward transport in the eastern boundary current system.

Plain Language Summary The Rockall Trough (RT) is a key pathway for warm and salty water flowing northward, a process which plays a key role in dictating the western European climate. However, the amount of water flowing northward, and how it changes over time, is still rather uncertain. In particular, the narrow boundary current in the eastern RT has previously proven difficult to measure. In this paper, we use 6 years of continuous oceanographic observations in the RT to monitor the flow. We also used underwater robots, called gliders, to focus on the narrow current in the eastern boundary. The data gathered give the best description of the ocean currents in the region to date. The study period coincided with a period of profound change across the subpolar North Atlantic, with a strong freshwater signal detected in the RT around 2017. The glider observations give a detailed view of the narrow eastern boundary current and how it varies seasonally, and also revealed the presence of a southward-flowing current at depth.

1. Introduction

The Rockall Trough (RT, Figure 1) serves as a key pathway for the poleward transport of oceanic heat, salt, carbon and nutrients. In the eastern subpolar North Atlantic (SPNA) the North Atlantic Current (NAC) consists of several branches with the southeastern branch, the warmest and saltiest, flowing through the RT. In addition, Eastern North Atlantic Water flows from the Bay of Biscay into the RT along the continental shelf break in the European Slope Current (ESC) (Booth & Ellett, 1983; Holliday et al., 2015; Huthnance & Gould, 1989; Huthnance et al., 2022; Xu et al., 2015). Around 50% of the transport through the RT continues toward the Arctic via the Faroe-Shetland Channel (Berx et al., 2013), while the remainder either flows east into the North Sea (Marsh et al., 2017) or west into the Iceland Basin and recirculates in the Sub-polar Gyre (SPG) (Houpert et al., 2020). The RT therefore plays a crucial role in the meridional connectivity of the North Atlantic's eastern boundary current system, and can be considered the easternmost extension of the SPG. Furthermore, as transport

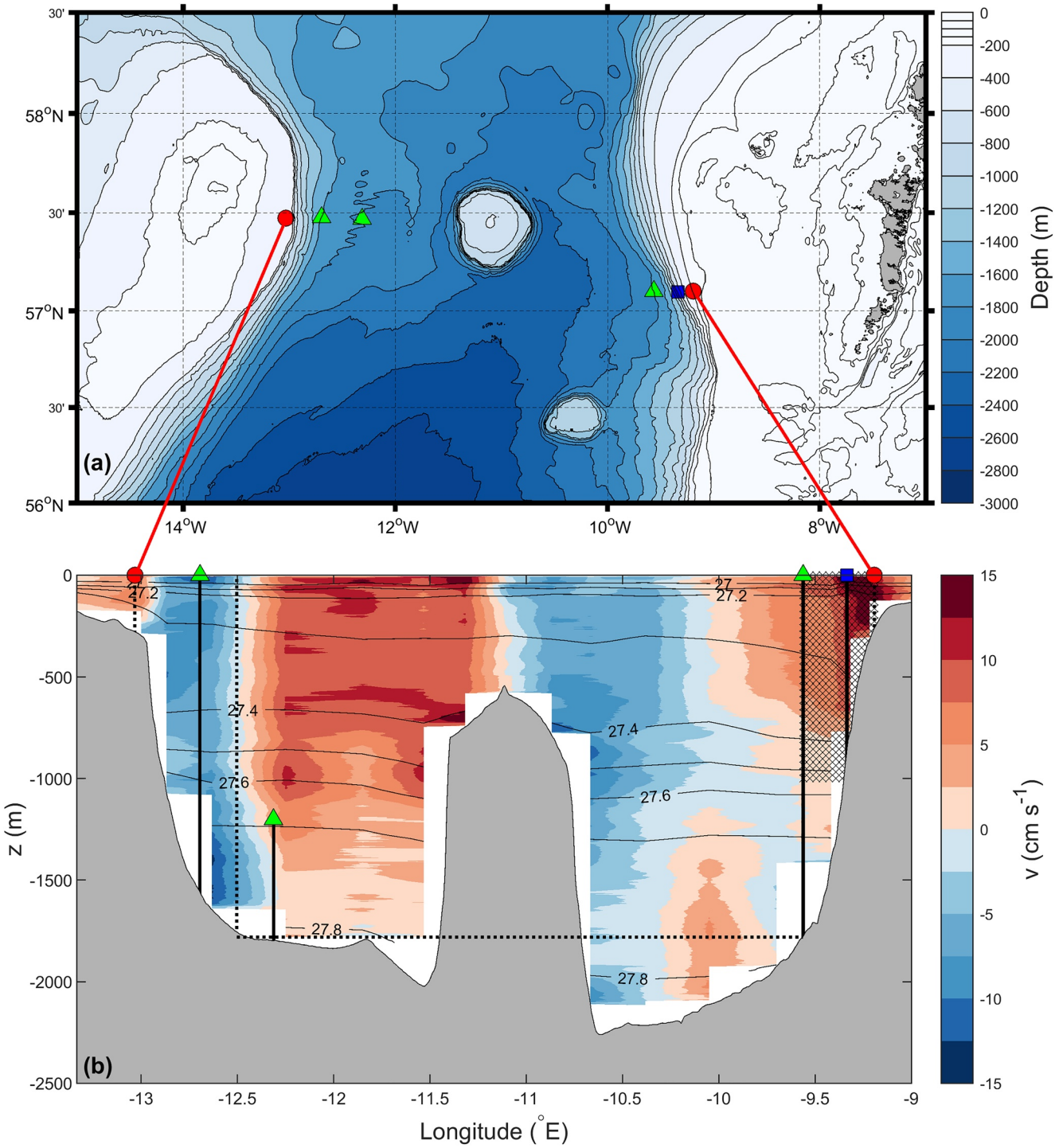

Figure 1. Bathymetry (a) and meridional velocity structure (b) of the Rockall Trough (RT) region west of Scotland, along with the positions of the Overturning in the Subpolar North Atlantic observing network. In each panel, green triangles show the locations of (from west to east) the WB1, WB2, and EB1 moorings, the blue square marks the acoustic Doppler current profiler location, and red circles show the nominal endpoints of the RT cross section. In panel (b), solid vertical black lines show mooring locations and the dotted vertical line at −12.5°E marks the partition between the western wedge and mid-basin regions, defined as the midway point between WB1 and WB2. Black cross-hatching in the upper 1,000 m of the eastern wedge denotes the region monitored by gliders. The color scale shows mean meridional (positive northward) velocity in the RT from 17 repeat lowered acoustic Doppler current profiler sections along the Extended Ellett Line in the period 1996–2017, while black contours show the corresponding potential density values (previously presented in Houpert et al. (2020)).

through the RT falls almost entirely into the upper limb ($\sigma_0 < 27.65$ kg m^{-3}) of the Atlantic Meridional Overturning Circulation (AMOC) (Li et al., 2021; Lozier et al., 2019), RT transport projects directly onto AMOC strength.

Repeat hydrographic observations on the Ellett Line, a section across the RT at approximately 57°N, began in 1975 (Ellett et al., 1986). Corresponding velocity observations began in 1996 with the establishment of the Extended Ellett Line (Holliday & Cunningham, 2013). The resulting synoptic velocity sections (Figure 1b) have revealed a highly barotropic (surface-to-seabed) southward flow at the western boundary (Houpert et al., 2020), which is thought to be due to an anticyclonic circulation around Rockall Bank (Dickson et al., 1986; Gary et al., 2018). At the eastern boundary, however, the mean flow is baroclinic, with weak flow near the seabed and a ∼15 cm s^{-1} ESC core centered over the upper slope. In the central RT the meridional flow is complex and changes sign due to interactions with topography, notably an anticyclonic circulation around Anton Dohrn Seamount, however the net flow is northward. Repeat hydrographic observations have resulted in RT geostrophic transport estimates of 3.7 ± 2.4 Sv for 1975–1998 (Holliday et al., 2000) and 3.0 ± 3.7 Sv for 1997–2014 (Holliday et al., 2015). The large uncertainties in these values reflect the limited capacity of synoptic sections to constrain the long-term mean due to the aliasing of large-amplitude mesoscale variability (Gary et al., 2018). This is illustrated by Holliday et al. (2018) who used ship-based hydrography and velocity sections to observe northward RT transports of 8.7 and −2.8 Sv in the summers of 2014 and 2016 respectively.

RT volume transport has been monitored continuously since 2014 using mooring observations under the wider Overturning in the Subpolar North Atlantic (OSNAP) array which spans the SPNA (Lozier et al., 2019). Houpert et al. (2020) reported the results for the first 4 years of OSNAP observations. The RT mid-basin (MB) transport was computed from hydrography via the thermal wind relation referenced to a level of no motion at 1,800 m, and had a mean value of 5.2 Sv. Moored current meters were used to estimate the transport at the western boundary, where the mean value was −2.0 Sv (positive northward). A bottom-mounted acoustic Doppler current profiler (ADCP) was deployed to monitor the ESC at the eastern boundary (Figure 1b), but the instrument was lost after only 8 months. As a consequence, numerical reanalysis model output was used to fill this part of the section (Houpert et al., 2020). Using model velocities which were bias-corrected using the available ADCP data, and incorporating current meter data, Houpert et al. (2020) found a mean eastern boundary transport of 1.4 Sv. The mean transport through the entire RT section (Figure 1b) was 4.5 Sv between 2014 and 2018. This value is higher than the estimates from 1975 to 2014 (Holliday et al., 2000, 2015), but broadly consistent given the large uncertainties associated with synoptic sections. Houpert et al. (2020) also revealed a −0.7 Sv year^{-1} trend and a significant seasonal cycle.

The eastern SPNA underwent unprecedented cooling and freshening in the mid-2010s which has been attributed to a deceleration of the northern NAC branches, which flow west of the Rockall Plateau, and an acceleration of the southeastern branch, which flows through the RT (Holliday et al., 2020). RT MB transport weakened by 1.0 Sv year^{-1} during 2014–2018 (Houpert et al., 2020) which may be evidence of the NAC circulation reverting to a pre-2010 state. However, continued monitoring is required to place this apparent weakening trend into a broader context. Density changes associated with these cooling and freshening events may project onto the RT MB transport via the thermal wind relation, but the response of the RT circulation to the large-amplitude hydrography changes over the wider North Atlantic (Fox et al., 2022; Holliday et al., 2020) remains unclear.

The ESC is driven by a combination of large-scale meridional density gradients and surface wind stress (Huthnance, 1984; Huthnance et al., 2020; Marsh et al., 2017). The flow is highly barotropic during winter months, when satellite altimeter results (Xu et al., 2015) reveal pronounced surface geostrophic flow along the shelf break. In summer, the ESC develops a significant baroclinic component (Souza et al., 2001) and the along-slope surface height signature becomes discontinuous and less prominent (Xu et al., 2015). The ESC is characterized by a high-salinity core centered over the 200 m isobath (Souza et al., 2001) and a narrow velocity core of ≥15 cm s^{-1} (Booth & Ellett, 1983; Souza et al., 2001) typically offset to the west, centered approximately over the 700 m isobath (Figure 1b). The strength and structure of the velocity core is variable, likely due to high-frequency wind forcing, and may therefore be poorly constrained by synoptic sections. For example, two summer hydrographic sections of the RT in 2014 and 2016 detected the salinity signature associated with the ESC, but the velocity signal was absent in both (Holliday et al., 2018). Furthermore, the fine-scale structure and elusive nature of the ESC raises questions over the ability of the relatively coarse numerical model used by Houpert et al. (2020) to capture the velocity field with sufficient accuracy and detail for transport monitoring.

In this study, we extend the four-year RT volume transport time series of Houpert et al. (2020) to 6 years (2014–2020), using the most recent OSNAP mooring observations. The new record offers insights into the interannual evolution of the RT circulation during a period of profound change across the eastern SPNA. We evaluate the impact of any interannual cooling or freshening signals by isolating the effects of temperature and salinity on geostrophic transport. In addition to this, we use 22 months of quasi-continuous glider observations (Figure 1b) to study the circulation in the eastern RT during the latter part of the record. While Houpert et al. (2020) relied heavily upon numerical model output and horizontal interpolation in the eastern RT, these 110 glider transects capture the circulation in this region in unprecedented detail. Their inclusion in the RT observing network therefore marks a transition away from the "patchwork" of observations and model output used previously toward a purely observational product.

2. Methods

2.1. Data

Three hydrographic moorings (WB1, WB2 and EB1) have continuously occupied the flanks of the RT between July 2014 and October 2020 as part of the wider OSNAP array (green triangles in Figure 1). Each mooring is equipped with Sea-Bird SBE37 MicroCATs conductivity, temperature, depths (CTDs) (measuring temperature, salinity, and pressure (p)) and Nortek Aquadopp current meters (measuring horizontal velocity (u, v) and p) distributed over the water column. WB1 and EB1 are full-depth moorings designed to measure the dynamic height difference across the RT. While EB1 sits at a water depth of ~1,800 m at the bottom of the steep continental slope, the relatively shallow angle at the base of the western boundary means WB1 sits at ~1,600 m (Figure 1b). The WB2 mooring is therefore added downslope of WB1 in order to capture hydrography, and hence dynamic height, down to ~1,800 m at the western boundary. A bottom-mounted ADCP was deployed in October 2014 at 750 m depth at the RT eastern boundary in order to monitor ESC velocity (blue square in Figure 1). The instrument returned only 8 months of data due to damage sustained by fishing activity. Temperature and salinity fields recorded at WB1, WB2 and EB1 were calibrated using seawater samples and in situ CTD profiles, corrected for sensor drift, converted to the conservative temperature and absolute salinity (Θ and S, SCOR (2010)), de-spiked, and then de-tided using a 48-hr lowpass filter. The (u, v) fields recorded at WB1, WB2 and EB1 were corrected for sound and magnetic deviation and then de-tided using a 48-hr lowpass filter. All fields were then interpolated linearly onto a 20 dbar vertical grid with a 12-hr temporal resolution. Data gaps at the surface were filled by repeating the topmost observed value vertically at each time step.

Four consecutive Seaglider missions occupied the eastern RT boundary region during the periods April–August 2020, October 2020–January 2021, April–May 2021, and October 2021–February 2022. The instruments completed a total of 110 repeat transects between the approximate EB1 mooring location and the 200 m isobath to the east (cross-hatched region in Figure 1b). Gliders travel with a saw-tooth trajectory between the surface and the seabed up to a maximum depth of 1,000 m, navigating with a magnetic compass while underwater and obtaining a Global Positioning System (GPS) position fix when on the surface. They record Θ, S and p along their path and, based on any deflection off course between consecutive GPS fixes, can estimate the mean horizontal velocity vector, $(\overline{u}, \overline{v})$, for each dive. Since vertical velocity shear is generally far greater than horizontal velocity shear on the scale of a single glider dive, $(\overline{u}, \overline{v})$ can in practice be considered a depth-averaged current vector. On the eastern (shelf) side of each transect, gliders were programmed to surface on alternate dives to mitigate the risk of collisions with boat traffic, and a single $(\overline{u}, \overline{v})$ vector was calculated for each dive pair. The glider CTD sensor and compass were calibrated before each mission, and an in-water compass calibration was performed at the start of each mission when the glider first left the shelf. Coefficients of the gliders hydrodynamic flight model (Eriksen et al., 2001) were re-calculated after each mission by selecting a subset of dives and iteratively comparing the vertical velocity predicted by the flight model against the vertical velocity implied by the pressure sensor. The flight model was then used to compute $(\overline{u}, \overline{v})$ and correct for thermal inertia effects on the CTD sensor. Θ and S data were reviewed and vertical profiles smoothed in GliderTools (Gregor et al., 2019).

Meridional velocity fields from the GLORYS12V1 reanalysis product for the eastern RT boundary region between July 2014 and October 2020 were obtained from the Copernicus Marine and Environment Monitoring Service (CMEMS). GLORYS21V1 is a global ocean eddy-resolving (1/12° horizontal resolution, 50 vertical levels) reanalysis covering the altimetry period (1993 onward). We obtained satellite-derived absolute dynamic topography, η, from CMEMS. These data are gridded at a 1/8° horizontal resolution with a daily temporal resolution.

Gridded bathymetry data were obtained at 30 arc-second resolution from the General Bathymetric Chart of the Ocean (GEBCO).

2.2. Volume Transport Calculation

There are two aspects to the RT volume transport calculation. In Section 2.2.1 the transport is calculated from OSNAP moorings and GLORYS12V1 output following Houpert et al. (2020) between July 2014 and October 2020. For this purpose, the RT section is split into three subsections: the western wedge (WW), MB, and eastern wedge (EW). In Section 2.2.2 we recompute the transport in the EW subsection using glider data from the period between April 2020 and February 2022.

The general approach for computing volume transport, Q, is to spatially integrate the velocity field:

$$Q = \int_{-H}^{0} \int_{x_1}^{x_2} v(x, z) dx dz, \tag{1}$$

where v is the velocity component perpendicular to the section, x and z are the along-section and depth coordinates, x_1 and x_2 are the section endpoints, and H is water depth. In practice, $v(x, z)$ is constructed differently for each subsection due to varying topography and instrumentation.

2.2.1. RT Transport From Moorings and GLORYS12V1 Output

The methodology for calculating volume transport from the RT mooring array is largely consistent with Houpert et al. (2020). Here, we briefly outline the method and highlight any departures from the previous approach.

We define the WW as the zonal subsection bounded by the western endpoint of the section and the midpoint between WB1 and WB2 (WB1/2 hereafter, Figure 1b). The WW velocity field is constructed using meridional velocity values from the WB1 current meters. East of WB1, we repeat the velocity profile eastward to WB1/2 to reflect the horizontally uniform flow observed by ship-based observations (Figure 1b). Moving west from WB1, velocities deeper than 250 m are tapered linearly to zero at the seabed, while velocities shallower than 250 m are tapered linearly to reach zero at −12.9°E. This procedure ensures the northward jet over Rockall Bank (centered around −13°E, Figure 1b) is omitted from our calculation. Meridional velocity values from the WB2 current meters are used to fill the region east of WB1/2 below 1,600 m, however the flow over this small area is weak and contributes negligibly to transport.

We define the MB subsection as the area between WB1/2 and EB1 (Figure 1b), and compute the MB transport from the dynamic height difference across the section. To generate a WB1/2 hydrographic profile, WB1 Θ and S values are used above 1,600 m while WB2 Θ and S values are used below 1,600 m. This horizontal displacement of hydrographic data is justified by the fact the isopycnals are relatively flat between WB1 and WB1/2 (Figure 1b), meaning the transport here would not be captured by baroclinic shear. The dynamic height profiles at both WB1/2 and EB1 are then computed relative to 1,760 m, the deepest shared depth level, and the transport per unit depth at each depth level is given by their difference. In contrast to the approach of Houpert et al. (2020), we do not attempt to adjust MB transports to account for the diminished cross-sectional area due to the presence of the Anton Dohrn seamount (Figure 1b). To illustrate why, consider two curved sections connecting WB1/2 and EB1, one which arches northward around the seamount and another which passes to the south. By continuity, the transport through each section must be equal both to each other and to the transport through our straight section passing over the seamount. The transport is therefore uniquely defined by the difference in dynamic height between the two moorings and is not diminished by the presence of the seamount.

We define the EW as the zonal subsection between EB1 and the eastern endpoint of the section (Figure 1b), and construct the EW velocity field from the EB1 current meters, the 8-month moored ADCP record, and GLORYS12V1 output. GLORYS12V1 was previously found to capture the meridional velocity variability recorded by the ADCP during its 8-month occupation, but systematically underestimated the strength of the flow by ∼7.6 cm s^{-1} (Houpert et al., 2020). To overcome the scarcity of ADCP observations, we generate a 6-year, virtual ADCP by interpolating the GLORYS12V1 velocities onto the ADCP location and bias-correcting by adding the inferred 7.6 cm s^{-1} offset. In the region to the west of the ADCP location and shallower than 750 m, the velocity field is linearly interpolated between EB1 current meter values and the virtual ADCP values. Moving east from the ADCP location the flow is tapered linearly to reach zero at −9.2°E, the eastern section endpoint (the

flow may be non-zero at the seabed). Below 750 m, EB1 current meter values are repeated horizontally eastward into the seabed. EW transport estimates computed using the method outlined above are heavily dependent on the bias correction applied to GLORYS12V1 output. As this bias is established over a single 8-month period, it is not clear whether the method is appropriate for monitoring EW transport variability over seasonal to interannual time scales. This issue was a central motivation to start monitoring the EW using gliders.

2.2.2. EW Transport From Gliders

The 110 glider transects of the EW were intended to follow a common trajectory approximately perpendicular to isobaths. However, glider transects are invariably affected by the ocean velocity field and hence follow irregular and inconsistent trajectories. As a result, different transects do not correspond spatially and, due to the variability in slope shape and steepness at different locations, do not in general have the same cross-sectional area. We develop a novel technique to overcome this issue: all transects are projected onto a common section, the EW zonal subsection, using an along-isobath transformation. The underlying assumption is that ESC streamlines follow isobaths (Booth & Ellett, 1983; Huthnance et al., 2020; Souza et al., 2001), and hence tracers are conserved along isobaths over these lengthscales (∼30 km).

The EW subsection (black line in Figure 2a) has horizontal coordinate x and vertical coordinate z. As bathymetry, H, is monotonic in x (Figure 2b) we can define a function f such that $H = f(x)$ and $x = f^{-1}(H)$. For a given glider transect, we define the along-path horizontal coordinate s and calculate $H(s)$ at each point. An x-coordinate is then assigned to each point s using the mapping

$$x \equiv f^{-1}(H(s)). \tag{2}$$

Note that $H(s)$ need not be monotonic. This transformation is analogous to taking points on the path s and sliding them continuously along isobaths until they reach the EW subsection (Figure 2a). We map scalar hydrography values onto the section directly:

$$\Theta(s, z) \rightarrow \Theta(x, z) \tag{3}$$

$$S(s, z) \rightarrow S(x, z). \tag{4}$$

From the resulting fields we also compute potential density, $\sigma_0(x, z)$. The horizontal spacing between adjacent Θ-S profiles may change under this transformation (since $\frac{\partial H}{\partial s} \neq \frac{\partial H}{\partial x}$ in general). However, the geostrophic transport between the two profiles is not affected as this depends on their dynamic height difference only, not their separation.

To compute the volume transport through each glider transect we first define $\overline{v}_\perp(s)$, the component of $(\overline{u}, \overline{v})$ locally perpendicular to the path s. Under our transformation from s-space to x-space, $\overline{v}_\perp(s)$ becomes a meridional vector component associated with each x position, $\overline{m}(x)$:

$$\overline{v}_\perp(s) \rightarrow \overline{m}(x). \tag{5}$$

For the transformation to conserve transport we multiply locally by $\frac{\partial s}{\partial x}$ to find the depth-averaged meridional velocity, that is,

$$\overline{v}(x) = \overline{m}(x)\frac{\partial s}{\partial x}. \tag{6}$$

This ensures that the volume transport, Q, between two given isobaths, H_1 and H_2, is the same in either coordinate system:

$$Q = \int_{s_1}^{s_2} H(s)\overline{v}_\perp(s)ds = \int_{x_1}^{x_2} H(x)\overline{m}(x)\frac{\partial s}{\partial x}dx = \int_{x_1}^{x_2} H(x)\overline{v}(x)dx, \tag{7}$$

where s_n is defined by $H_n = H(s_n)$ and $x_n \equiv f^{-1}(H_n)$. In the rare instances where the glider path is approximately parallel to isobaths, $\overline{v}_\perp(s)$ is oriented perpendicular to isobaths and the factor $\frac{\partial s}{\partial x}$ approaches $\pm\infty$. We combat this by manually imposing $-4 \leq \frac{\partial s}{\partial x} \leq 4$, with values outside this interval mapped to the limit values. This introduces a small error in the velocity field transformation, but as the omitted transport is perpendicular to isobaths it is not our primary focus. The limit values of ± 4 are selected by trial-and-error to minimize the error in Equation 7.

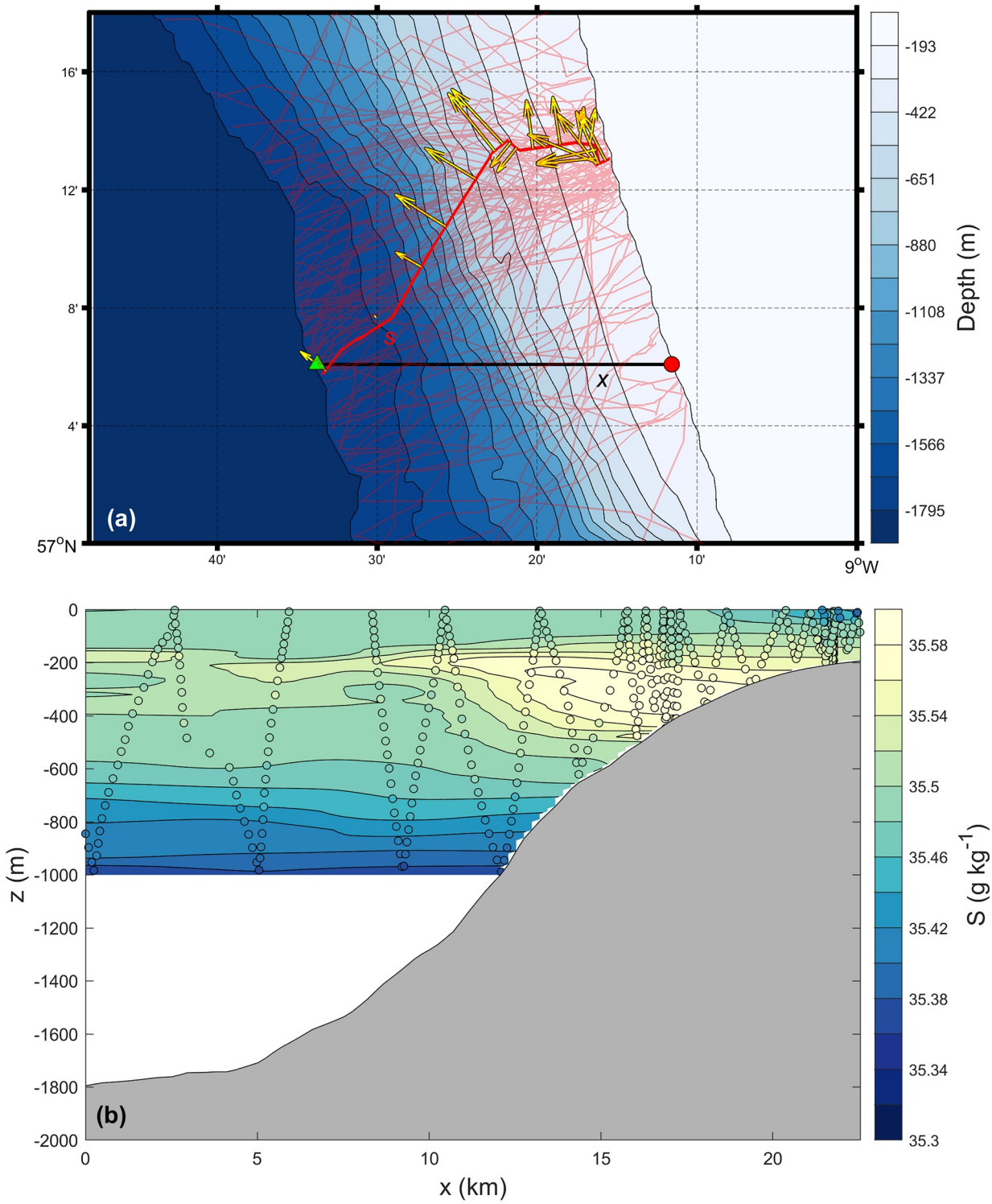

Figure 2. Gridding of glider data in the Rockall Trough eastern wedge (EW). Panel (a) shows isobaths between the EB1 mooring location (green triangle) and the eastern section endpoint (red circle). The bold black line denotes the EW subsection, with along-section coordinate x. Glider transects are shown by faint red lines, and have along-section coordinate s. A transect from 03 December 2020 is highlighted in bold red as an example, with yellow arrows denoting the perpendicular component of depth-averaged velocity, $\overline{v}_{\perp}(s)$. Panel (b) demonstrates Barnes (1994) interpolation onto the standard zonal section. In this example we show S values from the same 03 December /2020 transect shown in (a). Scattered points show every 25th glider observation mapped onto the EW section using the along-isobath transformation, while colored contours show interpolated field. Note the one-to-one correspondence between x coordinate and bathymetry.

The transformed Θ and S values on the standard zonal section are interpolated onto a two-dimensional grid with horizontal and vertical resolutions $dx \approx 250$ m and $dz = 10$ m respectively using the Barnes (1994) objective analysis method (Figure 2b). Transformed depth-averaged meridional velocities, $\overline{v}(x)$, are also interpolated using the Barnes (1994) method but in the x-direction only. We employ horizontal and vertical smoothing length scales of 3 km and 10 m respectively.

In order to study the two-dimensional velocity structure on our common zonal section, we compute the meridional component of baroclinic velocity relative to the sea surface, v_0, using the gridded σ_0 values via the thermal wind relation. We find a barotropic reference velocity by imposing the constraint that upon depth-averaging the meridional velocity field must equal the glider-derived depth-averaged meridional velocity $\overline{v}(x)$, that is,:

$$v(x,z) = v_0(x,z) - \frac{1}{H}\int_{-H}^{0} v_0(x,z)dz + \overline{v}(x) \tag{8}$$

We also compute an alternative velocity field, v_η, by referencing v_0 to the surface geostrophic flow from absolutely dynamic topography, η. First η is interpolated onto the glider path s to find $\eta(s)$ for each transect. We then obtain $\eta(x)$ using our along-isobath transformation (Equation 2), and solve for v_η using

$$v_\eta(x,z) = v_0(x,z) + \frac{g}{f}\frac{\partial \eta}{\partial x}(x). \tag{9}$$

where g is the local acceleration due to gravity and f is the local Coriolis frequency.

3. Results

3.1. Hydrography

The 6-year mean Θ, S and σ_0 profiles measured by the WB1/2 and EB1 moorings are shown in Figures 3a, 3c, and 3e. The RT is typically ∼0.04 g kg^{-1} saltier at the eastern boundary at depths shallower than 1,300 m. The RT is also warmer at the eastern boundary in the mid-water column, with a maximal zonal Θ difference of ∼0.7°C at ∼1,000 m depth. However, this zonal Θ difference decreases to near zero both below 1,300 m and at the surface.

Figures 3b, 3d, and 3f show temporal means of the two-dimensional gridded glider hydrography sections, Θ(x, z), $S(x, z)$ and $\sigma_0(x, z)$. Isotherms, isohalines and isopycnals all slope down toward the slope over the mid-water column, and a high-salinity ($S > 35.5$ g kg^{-1}) core sits at the top of the slope at around 300 m depth. The westernmost profiles, at $x = 0$, correspond to the EB1 mooring location and are plotted in Figures 3a, 3c, and 3e for direct comparison with the EB1 mooring observations. Glider measurements resolve stratification in the upper 50 m that is not captured by the moorings as this is above the shallowest instrument.

While glider-observed Θ closely agrees with its mooring counterpart (Figure 3a), glider-observed S appears biased low by ∼0.02 g kg^{-1} throughout the upper 1,000 m (Figure 3c). It is not clear to what extent this is caused by along-isobath S gradients versus issues with the glider conductivity sensor. Furthermore, as only the first glider mission coincides with the mooring deployment period, it is not clear whether this issue affects the subsequent glider missions. However, as Θ is the dominant control over density in this region, we do find a close agreement between mooring and glider σ_0 values when averaged over the concurrent time period (Figure 3e). Glider-observed S has a minimal influence on geostrophic velocity shear: repeating the thermal wind shear calculation with S held constant results in an ESC core velocity relative to the sea surface (v_0 in Equation 8) which is highly correlated ($r = 0.96$) with the equivalent field computed using the full, time-varying S field.

Figure 4 shows anomalies of mooring-based Θ and S relative to the long term means (Figure 3). Variability in Θ (Figures 4a and 4b) is dominated by the seasonal cycle which is led by the upper ∼200 m and is seen to propagate down through the water column. Other notable features are the cold anomalies at WB1/2 in the latter half of both 2015 and late 2016, and the warm anomaly at WB1/2 which persists at depth throughout 2017 (Figure 4a). Variability in S (Figures 4c and 4d) is dominated by interannual signals, most notably the transition from salty to fresh anomalies in the upper ∼1,000 m during the first 4 years of the record.

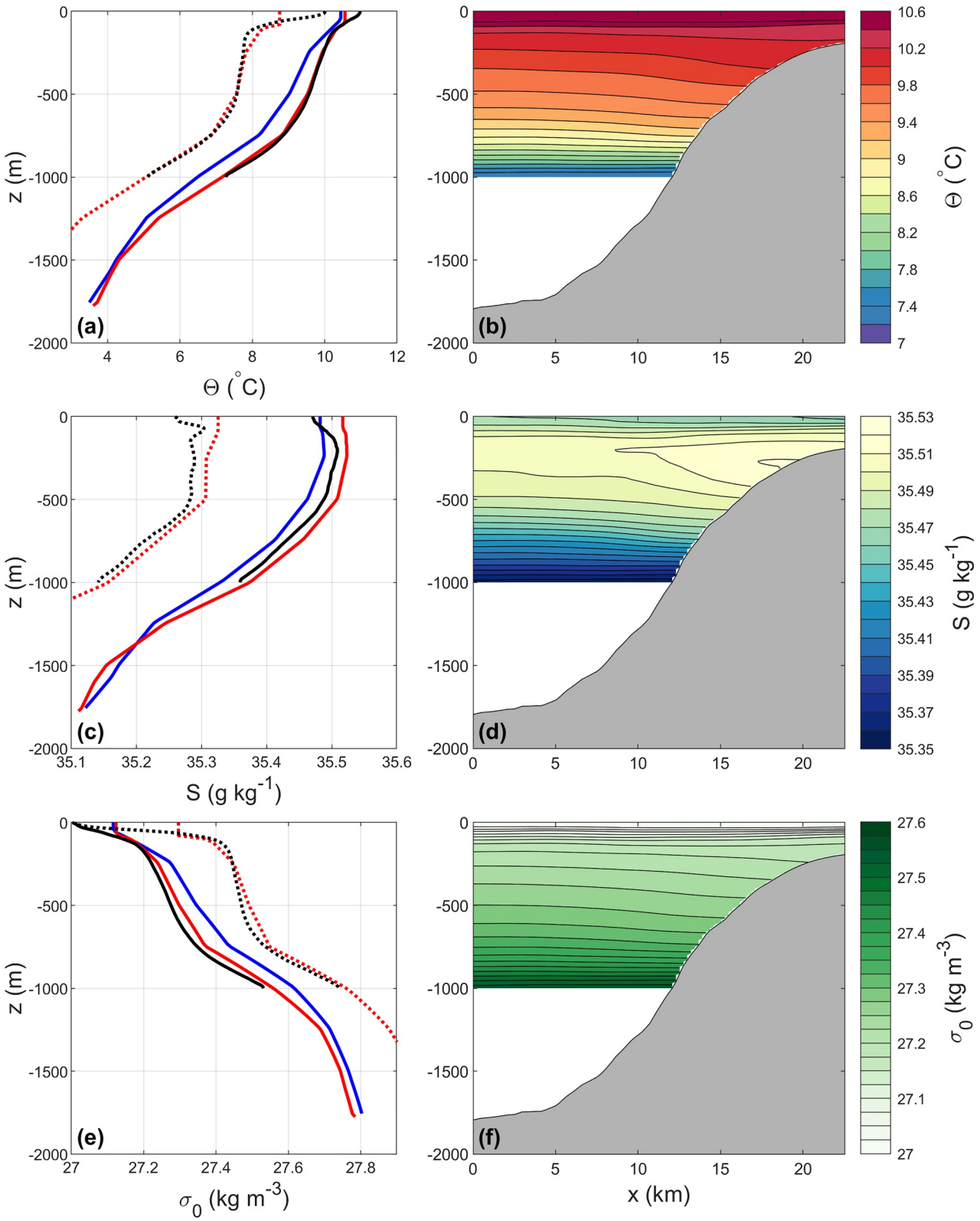

Figure 3. Panel (a) shows temporal mean Θ from WB1/2 (blue), EB1 (red), glider profile at EB1 (black). Dashed lines indicate means over the period when both the glider and EB1 were in the water, horizontally offset for clarity. Panel (b) shows temporal means of $\Theta(x, z)$ across the 110 gridded glider transects of the eastern wedge taken between April 2020 and May 2021. Panels (c and d) are as for panels (a and b) but show S while panels (e and f) show σ_0.

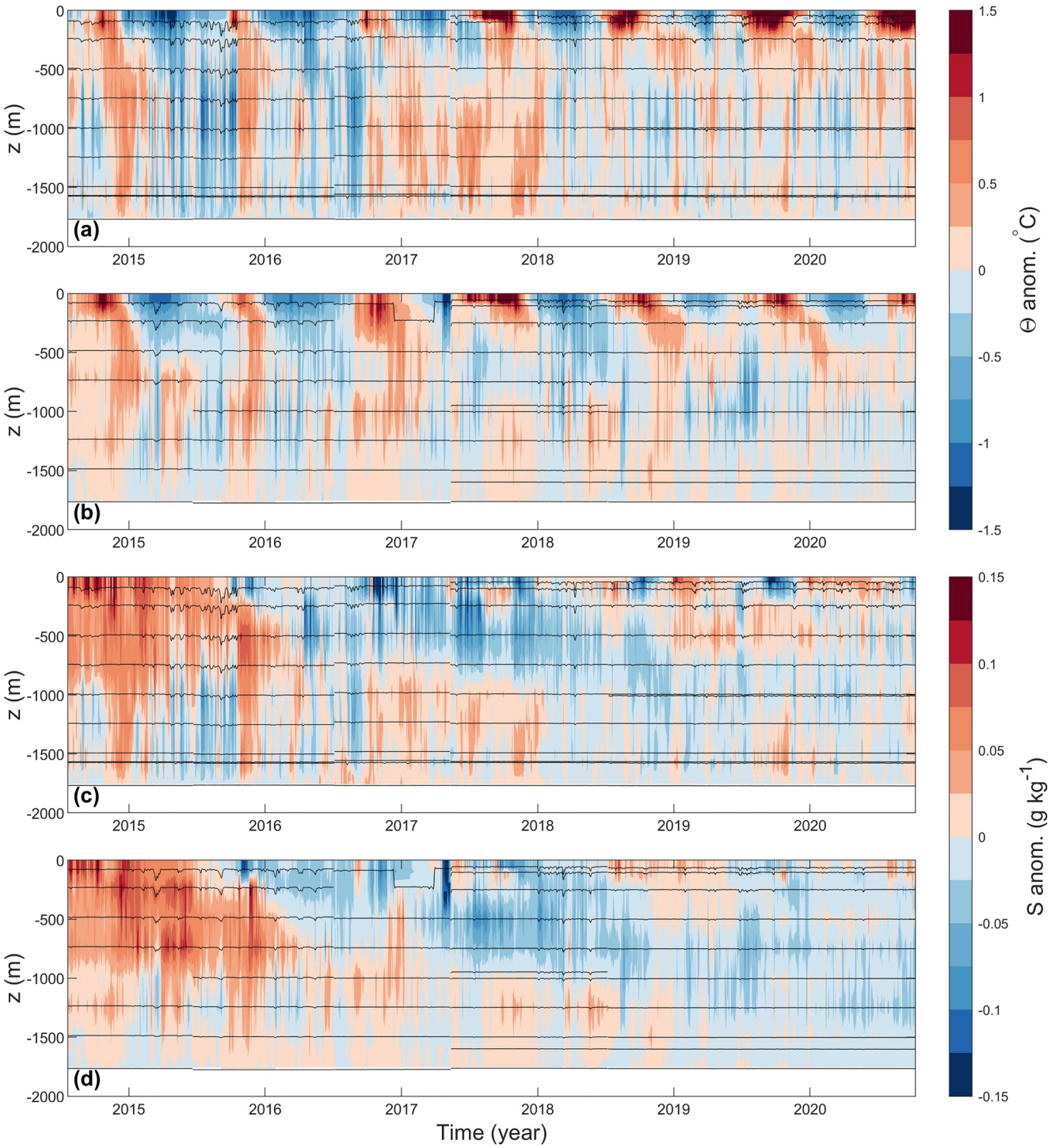

Figure 4. Panels (a and b) show temporal Θ anomalies, relative to the long term mean (Figure 3a), from the WB1/2 (a) and EB1 (b) moorings. Panels (c and d) are as for panels (a and b) but show *S* anomalies. Instrument depths are shown in black.

3.2. Velocity Structure and Variability

The mean meridional velocity fields constructed for the EW and WW from the RT mooring/model array are shown in Figures 5a and 5b. The southward flow in the WW is strongest (∼−9 cm s^{-1}) toward the base of the WB1 mooring. The adjusted GLORYS12V1 output at the ADCP location clearly dominates the northward flow in the EW, giving an effective ESC core of ∼16 cm s^{-1} centered over the 750 m isobath at ∼300 m depth. Deeper

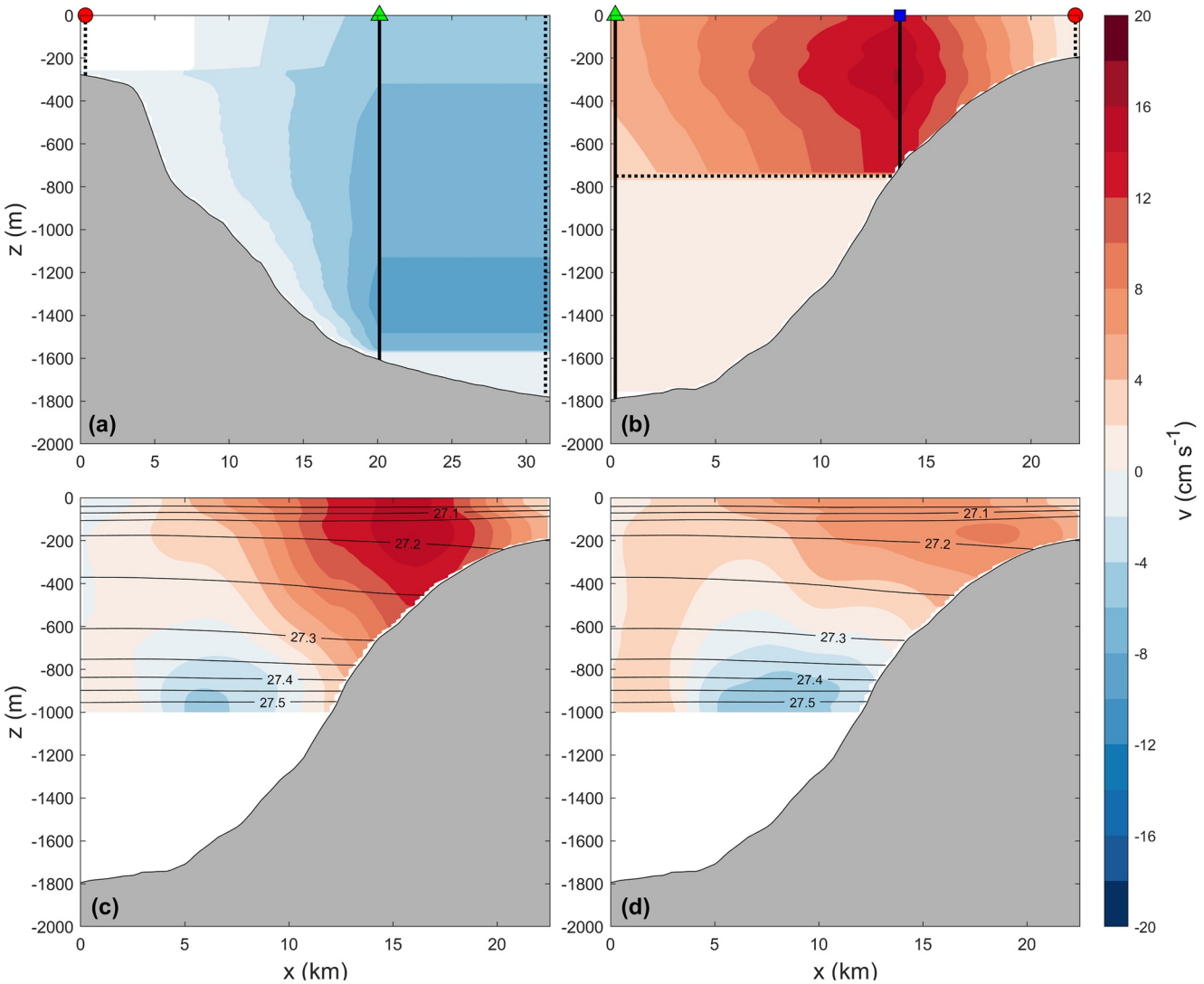

Figure 5. Panels (a and b) show the temporal mean meridional velocity field constructed for the (a) western wedge (WW) and (b) eastern wedge (EW) from the Rockall Trough mooring/model array. The WW field is computed from WB1/2 current meters, while the EW (b) field is computed from a combination of EB1 current meters and GLORYS12V1 output bias-corrected using acoustic Doppler current profiler (ADCP) data. Green triangles show the locations of the WB1 and EB1 moorings, the blue square marks the ADCP location, and red circles show the nominal section endpoints. Panels (c and d) show the temporal mean meridional velocity field across the 110 gridded glider sections of the EW taken between April 2020 and February 2022. Panel (c) shows $v\,(x,\ z)$ which is referenced using glider-derived depth-averaged velocity while panel (d) shows $v_\eta\,(x,\ z)$ which is referenced to satellite altimetry. Isopycnals are shown in solid black.

than 750 m the velocity field, derived solely from EB1 current meters, is weak and fails to capture any spatial structure.

Mean meridional velocity fields constructed from EW glider observations $v(x,\ z)$, referenced using glider-derived depth-averaged meridional velocity $\overline{v}(x)$ (Equation 8), and $v_\eta(x,\ z)$, referenced using satellite altimetry $\eta(x)$ (Equation 9), are shown in Figure Figures 5c and 5d. Note that $v(x,\ z)$ and $v_\eta(x,\ z)$ have identical baroclinic shear and differ only in their barotopic reference velocity. While $v(x,\ z)$ sees a ∼16 cm s^{-1} ESC current core centered over the 500 m isobath at ∼200 m depth (Figure 5c), the ESC from $v_\eta(x,\ z)$ is weaker and displaced shoreward, with an ∼8 cm s^{-1} current core centered over the 300 m isobath (Figure 5d). Both cases see southward mean flow below ∼800 m depth over the lower slope. However, as the gliders have a maximum operating depth of 1,000 m, the structure and strength of this subsurface countercurrent are not observed fully.

In order to isolate the effect of the different barotropic referencing methods used to compute $v(x,\ z)$ and $v_\eta(x,\ z)$, we plot the mean and standard error (SE) of both $\overline{v}(x)$ and $\overline{v_\eta}(x)$ (i.e., the depth-average of v_η) in Figure 6. Note

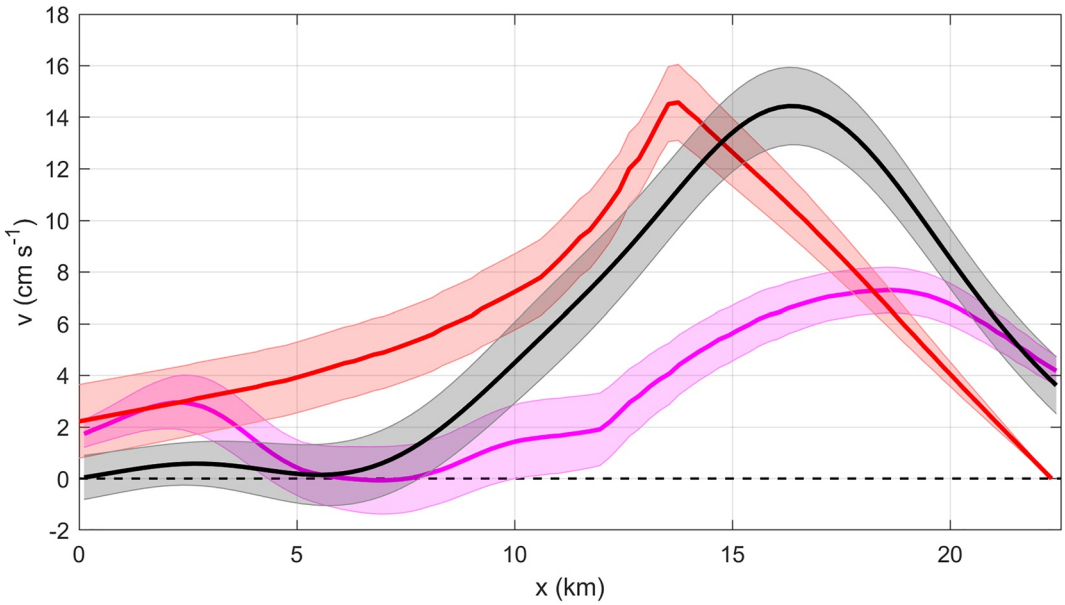

Figure 6. Temporal mean depth-averaged meridional velocities in the eastern wedge using three different methods. The depth average of the velocity fields shown in Figures 5b–5d are shown in red, black and magenta respectively. The shaded regions denote standard error, which is computed by dividing the standard deviation by $\sqrt{N_{\mathrm{DoF}}}$, the square root of number degrees of freedom. We treat each glider transect as an independent observation, so take $N_{\mathrm{DoF}} = 110$, whereas for mooring observations we compute N_{DoF} based on the time series autocorrelation.

that $\overline{v_\eta}(x)$ is not the same as the surface geostrophic velocity $\frac{g}{f}\frac{\partial \eta}{\partial x}(x)$ derived from satellite altimetry, although the two are related via Equation 9. The mean ±1 SE of $\overline{v}(x)$ over the upper slope ($x \approx 16$ km) is 14 ± 1.5 cm s^{-1} whereas the equivalent values for $\overline{v_\eta}(x)$ are 7 ± 1 cm s^{-1}, indicating that v_η underestimates both the strength and the variability in the ESC core. Variability in both $\overline{v}(x)$ and $\overline{v_\eta}(x)$ is maximal over the mid-slope at $x \approx 11$ km.

Seasonal composites of $v(x, z)$ and $\sigma_0(x, z)$, generated by temporally averaging the glider transects during winter (DJF, 42 transects), spring (MAM, 24 transects), summer (JJA, 18 transects), and autumn (SON, 26 transects), reveal a marked seasonality in the strength and structure of the EW velocity field (Figure 7). The ESC is strongest and broadest during spring, when it reaches ∼30 cm s^{-1}, and weakest during winter and summer, when the current core is ∼10 cm s^{-1}. A relatively small but defined ESC core of ∼20 cm s^{-1} is seen in autumn. In winter and spring, when stratification is weak, the ESC core extends upwards to the surface, whereas summer and autumn see a subsurface core beneath the shallow pycnocline. Evidence for a countercurrent is visible in all seasons, particularly during winter when the current appears broader, shallower and stronger ($v = -11$ cm s^{-1} at $z = -800$ m). During the other three seasons the countercurrent is only partially captured due the gliders' 1,000 m depth limit.

3.3. Mean Volume Transport

The 6-year mean ±1 SE volume transports through the WW, MB, and EW subsections as measured by the RT mooring/model array were $Q_{WW} = -1.8 \pm 0.3$ Sv, $Q_{MB} = 5.5 \pm 0.5$ Sv, and $Q_{EW} = 1.3 \pm 0.2$ Sv. The mean volume transport through the full RT section was $Q_{RT} \equiv Q_{WW} + Q_{MB} + Q_{EW} = 4.9 \pm 0.6$ Sv, compared to the 4.5 ± 0.8 Sv reported by Houpert et al. (2020) for the first 4 years of the record. The mean transport over the first 4 years of our time series was also 4.5 ± 0.8 Sv, indicating that our revised method of ignoring the Anton Dohrn seamount for the MB cross-sectional area calculation has negligible impact in practice. Figure 8a shows the temporal mean and SE of the volume transport through each RT subsection accumulated upwards from the seabed.

The mean ±1 SE of the upper-1,000 m volume transport in the EW recorded by the 22-month glider occupation and referenced using $\overline{v}(x)$ was $Q_{\overline{v}} = 0.7 \pm 0.2$ Sv, whereas the volume transport referenced using $\eta(x)$ was only $Q_\eta = 0.4 \pm 0.1$ Sv. Figure 8b shows the temporal mean and SE of $Q_{\overline{v}}$ and Q_η accumulated upwards from 1,000 m.

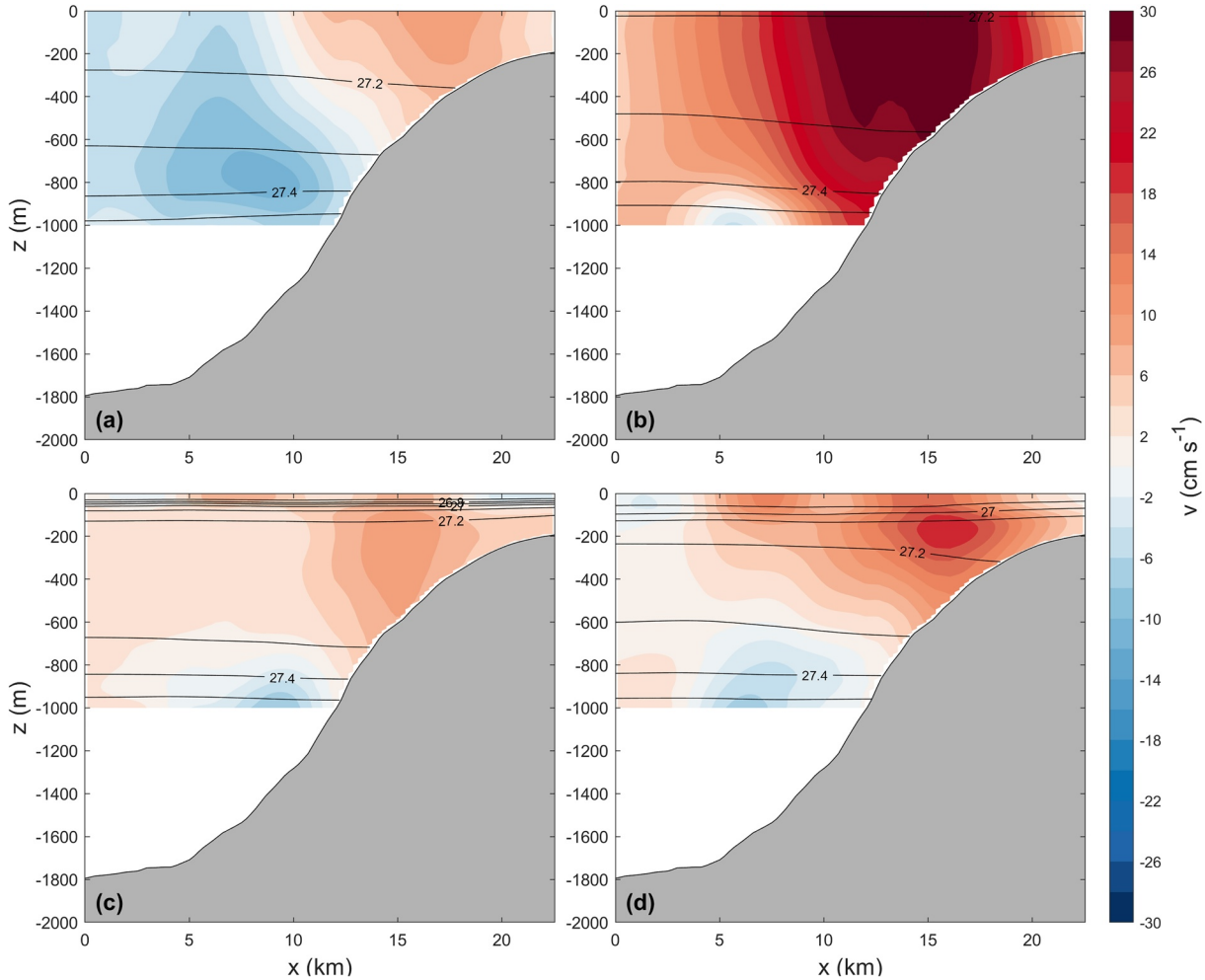

Figure 7. Seasonal composites of meridional velocity, $v(x,\ z)$, from gridded glider sections during (a) winter (DJF, 42 transects), (b) spring (MAM, 24 transects), (c) summer (JJA, 18 transects), and (d) autumn (SON, 26 transects). Corresponding isopycnals are shown in solid black.

For a direct comparison between glider and mooring/model observations we consider only EW transports in the upper 1,000 m during the period in April–August 2020 when both platforms were in the water. This yields mean transport values of $Q_{EW} = 1.6$ Sv, $Q_{\overline{v}} = 1.1$ Sv, and $Q_{\eta} = 0.4$ Sv. Note that 97% of the mooring/model-derived EW transport is in the upper 1,000 m, so the omission of the deep flow has a negligible impact on transport estimates in practice (Figure 8b). In summary, the glider-derived depth-averaged velocity observations suggest a lesser EW transport than the mooring/model array, while the transport derived from satellite altimetry is smaller still.

3.4. Volume Transport Variability

The 6-year time series for Q_{WW}, Q_{MB} and Q_{EW} are shown in Figure 9a, while the time series for Q_{RT} is shown in Figure 9b. The -1.0 Sv year^{-1} weakening trend in MB transport identified by Houpert et al. (2020) during the first 4 years has not continued into the final 2 years. Instead, we see a partial recovery toward the >5 Sv values which dominated the early record and no significant 6-year trend as a consequence. No significant trends were detected in Q_{WW} or Q_{EW}, but we note that the incidences of intense southward flow in the WW ($Q_{WW} < -10$ Sv) during 2015 remain exceptional.

From Figure 8a it is clear that Q_{MB} dominates the northward transport through the RT. To determine the controls on geostrophic circulation in the MB, we recompute Q_{MB} while holding either Θ or S constant at their respective temporal mean values (Figure 9c). Since Θ is the dominant control over density in this region, we find that varying only Θ explains 97% of the variance of the full Q_{MB} signal. The signal from varying only S is smaller in

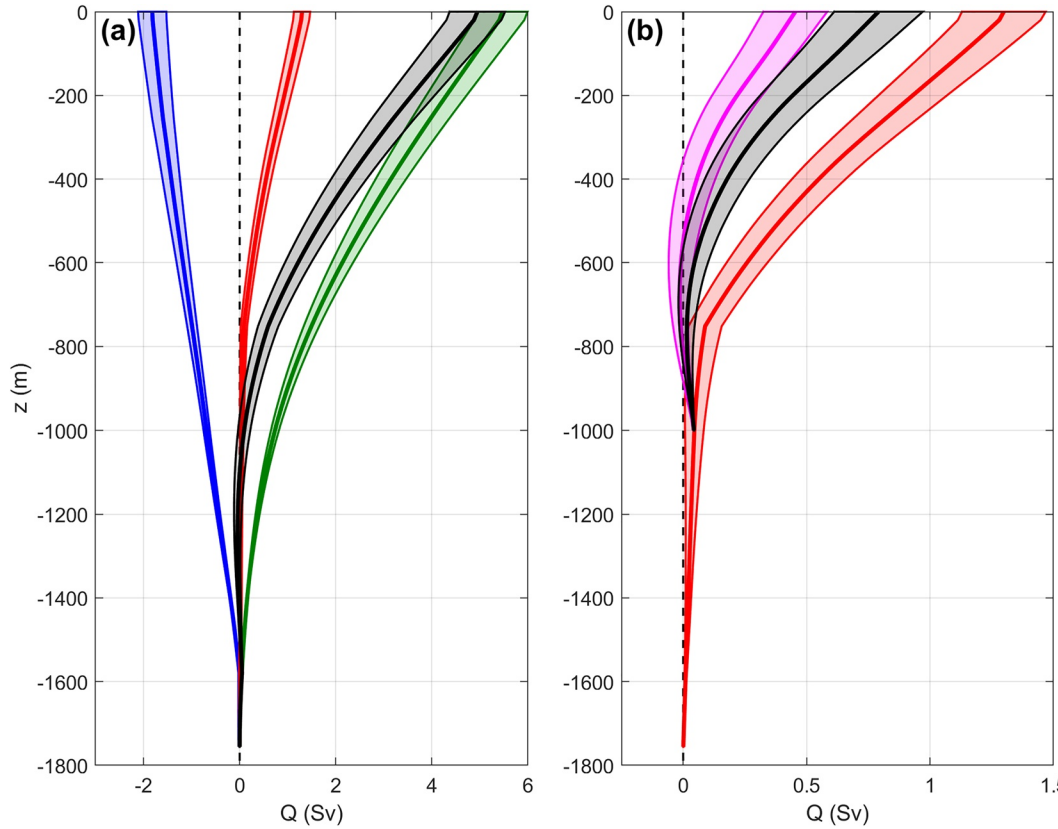

Figure 8. Temporal mean of volume transport, Q, accumulated upwards from the base of each subsection. Panel (a) shows Q_{WW} (blue), Q_{MB} (green), Q_{EW} (red) and their sum, Q_{RT} (black). Panel (b) shows $Q_{\bar{v}}$ (black) and Q_{η} (magenta) integrated from the Q_{EW} value of 0.05 Sv at $z = -1{,}000$ m, with Q_{EW} shown again for context. The shaded regions denote standard error.

amplitude and explains −77% of the variance, and therefore generally acts to dampen the Q_{MB} signal driven by changes in Θ (due to the high covariance between Θ and S in this region). Investigating further, we find that varying Θ only at WB1/2 (while keeping S fixed on both profiles) explains 76% of the variance in Q_{MB}, while varying Θ only at EB1 explains only 51%. The role of the WB1/2 Θ in governing Q_{MB} is evident from Figure 9d, though the relationship appears weaker toward the start of the record. In short, variability in Θ at the western boundary is a dominant control on the geostrophic circulation in the RT and, by extension, northward volume transport.

Time series for $Q_{\bar{v}}$ and Q_{η} are shown in Figure 10, with Q_{EW} shown again for reference. There is some qualitative agreement between the three time series, which all see a general decline through May–June 2020 before an increase in July. $Q_{\bar{v}}$ and Q_{η} also consistently suggest a weakened and often reversed flow in December–January of both observed winters. However, the $Q_{\bar{v}}$ signal is generally of greater amplitude than Q_{η}, particularly during the April–May maxima and the December 2020 minimum which Q_{η} fails to replicate. In April–May 2021, $Q_{\bar{v}}$ often exceeds 4 Sv and reaches a maximum value of 7.8 Sv.

Following Houpert et al. (2020), we construct monthly climatologies from each 6-year transport time series (Figure 11a). The range of the seasonal cycle in the EW and WW are 2.3 and 1.2 Sv, consistent with the first 4 years (Houpert et al., 2020). However, the MB seasonal range has decreased from 3.5 to 2.1 Sv with the extension of the time series. The seasonal range for the full RT section is 3.0 Sv, decreasing from 3.4 Sv over the first 4 years. The variance explained by the seasonal cycle is 20%, 23%, and 27% in the WW, MB, and EW respectively, and 25% for the full RT section.

The glider-derived transports in the EW, particularly $Q_{\bar{v}}$, suggest a much more pronounced seasonal cycle, with peak transport in April–May and flow reversal in December–January (Figure 11b). However, as this record is only 22 months long and has no observations in March or September, the apparent seasonality may be contaminated by synoptic variability.

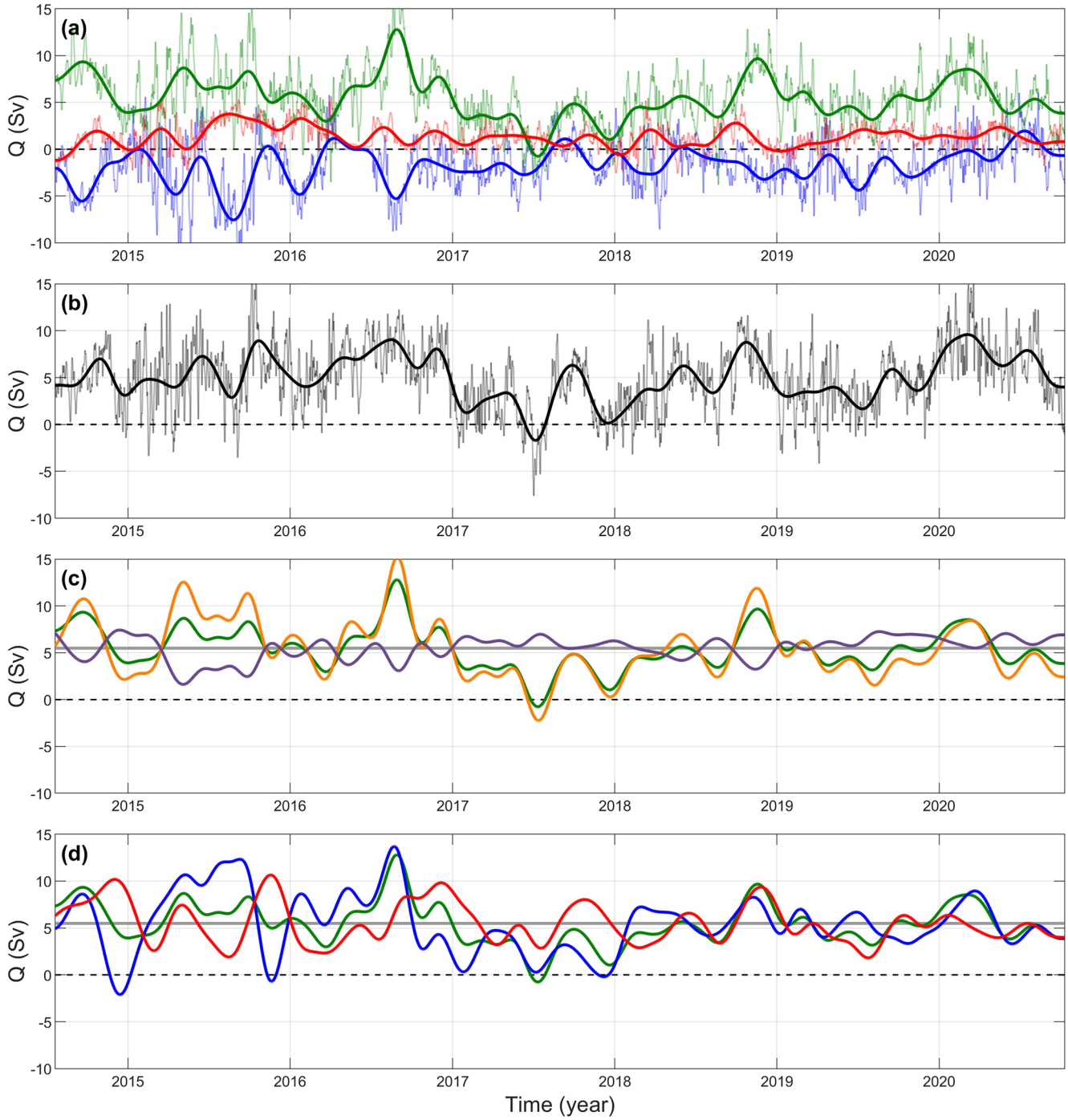

Figure 9. Six-year time series for volume transports Q_{WW} (blue), Q_{MB} (green), Q_{EW} (red) are shown in panel (a), while their sum Q_{RT} (black) is shown in panel (b). Narrow lines are the full temporal resolution fields while bold lines show 90-day low-pass filtered fields. Panel (c) shows 90-day low-pass filtered Q_{MB} computed by isolating changes in Θ (orange) and S (purple). Panel (d) shows equivalent fields calculated by isolating changes in Θ at WB1/2 (blue) and EB1 (red). The full Q_{MB} field, as shown in panel (a), is repeated for context in panels (c) and (d) (green), while its temporal mean value of 5.5 Sv is shown in gray.

4. Discussion

We have presented a 6-year observational record of meridional volume transport, Q, in the RT. This extension of the time series previously published by Houpert et al. (2020) provides new insights into the function of RT circulation in delivering, and modulating, poleward ocean transports on interannual time scales. In addition, we have incorporated glider observations into the RT observing array which capture the ESC, at the eastern flank of

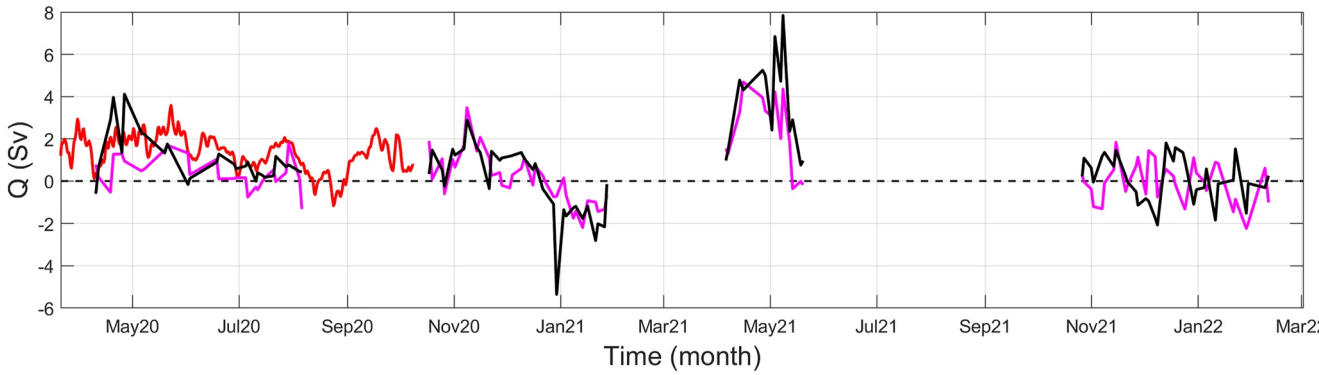

Figure 10. Time series' for volume transports, Q, in the eastern wedge: $Q_{\bar{v}}$ (black) is derived from glider hydrography referenced to glider depth-averaged velocity observations, Q_{η} (magenta) is derived from glider hydrography referenced satellite altimetry, and Q_{EW} (red) is derived from the mooring/model array.

the RT, in unprecedented detail. The glider data, together with novel analysis techniques, reveal both the mean state and seasonal variability in ESC velocity structure and volume transport.

4.1. The RT Circulation in a Changing North Atlantic

The 2014–2020 mean volume transport in the full RT section, $Q_{RT} = 4.9 \pm 0.6$ Sv, is toward the upper end of the range observed by previous hydrographic estimates of 3.7 ± 2.4 Sv for 1975–1998 (Holliday et al., 2000) and 3.0 ± 3.7 Sv for 1997–2014 (Holliday et al., 2015). Our value is also slightly greater than the 4.5 Sv mean reported by Houpert et al. (2020) during 2014–2018, which reflects the relatively high volume transports in the final 2 years of our record after a period of lower transport around 2017 (Figure 9b). This recovery in circulation strength, which is dominated by the signal in MB (Q_{MB}, Figure 9a), means that the -0.7 Sv year^{-1} weakening trend detected by Houpert et al. (2020) is no longer evident when considering the full 6-year time series.

The negative S anomalies observed on either flank of the RT around 2017 (Figures 4c and 4d) are evidence for the mid-2010s SPNA freshening signal (Holliday et al., 2020) propagating eastward into the RT. This coincides with a weakening of the northward geostrophic circulation (Q_{MB}, Figure 9a). However, we have demonstrated that S plays a secondary role in modulating RT circulation, and that changes in S actually promote a slight strengthening of the circulation around 2017 (Figure 9c). Instead, we identify Θ at the western boundary as the dominant control of RT circulation. Western boundary Θ promotes periods of weak Q_{MB} in late 2014, late 2015, and throughout 2017 (Figure 9d). However, the 2014 and 2015 signals are largely compensated by changes in Θ at the eastern boundary (Figure 9d), hence only the 2017 signal is manifested in Q_{MB}.

Examining the evolution of Θ at the western and eastern boundaries (Figures 4a and 4b) reveals that the 2014 and 2015 signals are associated with the breakdown of the warm summer mixed layer increasing the dynamic height on either side of the RT. The 2017 signal, however, is due to a persistent positive Θ anomaly which impacts only the western boundary below ~800 m (Figure 4a). Neither the spatial nor temporal structure of this anomaly are consistent with the breakdown of the summer mixed layer. This warming signal coincides with a period of oceanic heat convergence across the eastern SPNA (Desbruyères et al., 2021), indicating it was instead advected into the region horizontally. The subsequent recovery of Q_{MB}, and hence Q_{RT}, in 2018 was driven by western boundary Θ values reverting toward the mean. This suggests that the advection of subsurface Θ anomalies to the western boundary drives a leading mode of interannual variability in poleward RT volume transport.

4.2. New Perspectives on the ESC

Glider observations of the EW find the strength and structure of the ESC to be good agreement with previous results from the same region. For instance, the ~15 cm s^{-1} mean current core observed in the upper ~400 m (Figure 5c) is consistent with velocity structure reported by both Booth and Ellett (1983), Souza et al. (2001), and Huthnance et al. (2022). Furthermore, Souza et al. (2001) also observe a S maximum offset to the east of the velocity core (Figure 3d). This agreement indicates that glider depth-averaged velocity observations accurately measure the flow, and that the along-isobath transformation developed here preserves the key aspects of the velocity structure.

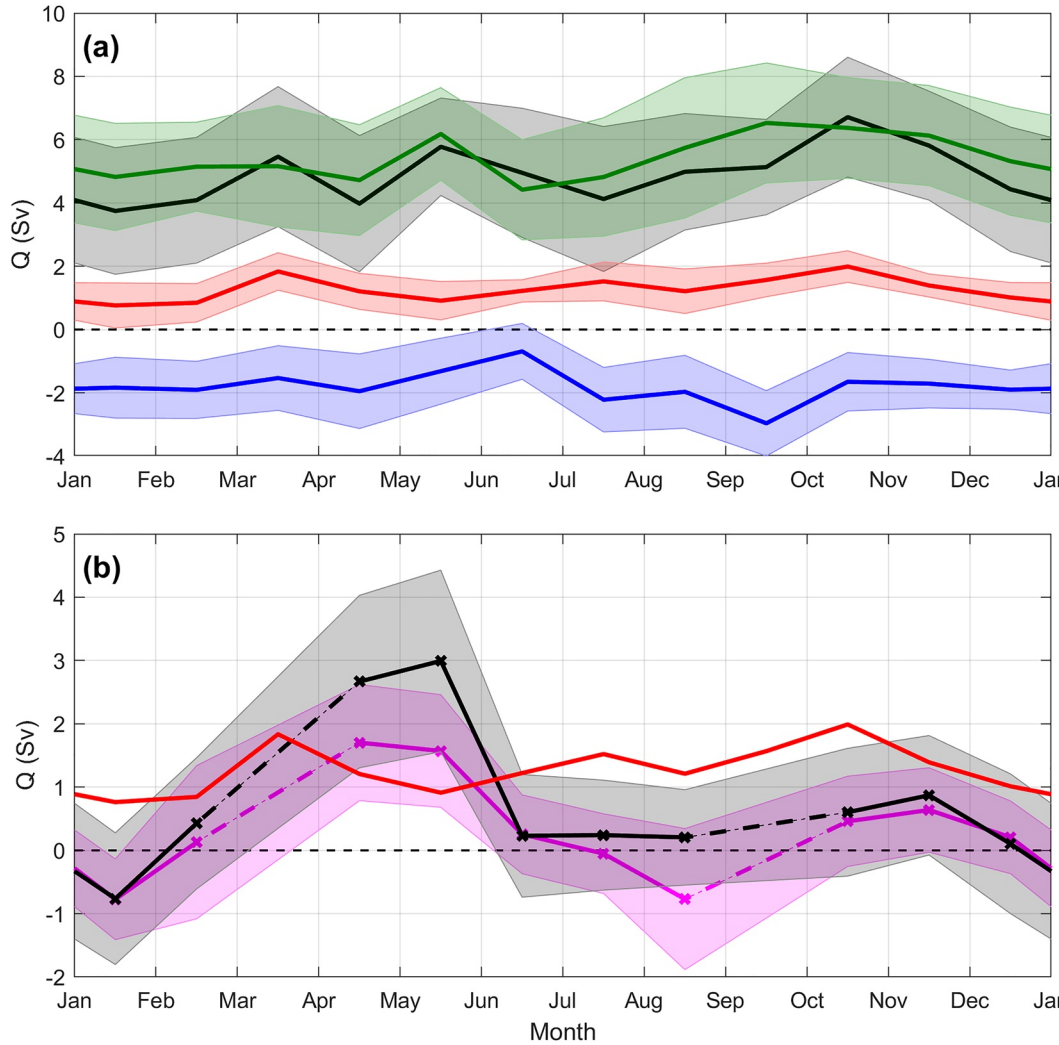

Figure 11. Monthly climatologies in volume transport, Q, for each subsection. Panel (a) shows Q_{WW} (blue), Q_{MB} (green), Q_{EW} (red) and their sum, Q_{RT} (black). Panel (b) glider-derived transports shows $Q_{\overline{v}}$ (black) and Q_{η} (magenta), with Q_{EW} shown again for context. Note that dashed lines indicate interpolated values for months (March and September) with no glider transects. Shaded regions denote standard error which is computed by dividing the standard deviation within each month by $\sqrt{N_{\mathrm{DoF}}}$. Glider transects are treated as independent measurements, so N_{DoF} is simply the number of transects in a given month. For mooring/model-generated transport, the monthly N_{DoF} is the number of degrees of freedom for the entire time series divided by 12.

The apparent seasonality in EW volume transport exhibits two maxima, in spring and autumn, and two minima, in summer and winter (Figure 11b). This seasonality is largely driven by changes in the strength of the ESC (Figure 7) and contradicts Xu et al. (2015) who find, based on satellite altimetry, that the ESC strength in our study region exhibits a simple seasonal cycle with a maximum in winter and a minimum in summer. The results of Xu et al. (2015) are consistent with seasonal stratification modulating ESC strength by altering the baroclinicity of the flow, whereas our results suggest a more complex relationship between the ESC and stratification strength. The depth-varying velocity fields (Figure 7) reveal that stratification has a profound effect on ESC structure, with summer and autumn exhibiting subsurface velocity maxima. It is therefore likely that Xu et al. (2015) underestimated the strength of the ESC in summer and autumn, and consequently detected a seasonality in the ESC surface signature which is inconsistent with the true seasonality of the ESC core. More broadly, this highlights a pitfall in using satellite altimetry to study boundary current seasonality without additional baroclinic shear information.

The gliders' ability to resolve two-dimensional flow structure, particularly below 750 m, has revealed the presence of a subsurface countercurrent over the lower slope (Figure 5). A similar feature can be seen in lowered

acoustic Doppler current profiler measurements taken further south at Goban Spur (Moritz et al., 2021), suggestive of meridional continuity, however the upstream origin of the countercurrent is unclear. This is a year-round feature of the circulation, but displays pronounced seasonality in position and strength (Figure 7). Strengthening and shallowing of the countercurrent in winter drives weakening and reversal of the EW transport (Figure 11b). Variability in the countercurrent is a previously unstudied mechanism for modulating the net northward flow in the EW. Gliders only partially capture the countercurrent structure due to their 1,000 m depth limit, therefore further observations at greater depth are required to characterize this feature fully.

Bias-corrected GLORYS12V1 output generates a realistic ESC core of around ∼15 cm s^{-1} (Figure 6), and appears to recreate certain aspects of the variability during the shared time interval (Figure 10). However, the method of linear interpolation in the horizontal (Figure 5b) poorly represents the complex velocity structure in the EW observed by gliders (Figure 5c), and it is not clear whether the variability is captured over longer timescales. The failure of Q_{EW} to resolve the southward flow in the countercurrent causes a 50% overestimation of EW volume transport relative to Q_v (Figure 8b). This highlights a more general issue with horizontally interpolating observed velocity values between adjacent profiles in regions of sloping topography.

We found that geostrophic velocity referenced to satellite altimetry, $v_\eta(x,\ z)$, underestimates the mean EW transport by ∼40% in comparison with referencing to depth-averaged velocity observations, $v(x,\ z)$ (Figure 5). This discrepancy is largely caused by a failure of $v_\eta(x,\ z)$ to capture the high transport in the spring (Figure 11b). The spatial resolution of gridded satellite altimetry is a known issue in this region (Houpert et al., 2020), however, as the ESC core is both broad and surface-intensified during spring (Figure 7b), one would expect a relatively pronounced surface signal easily detectable by satellite. Conversely in autumn, when the ESC core is narrow and subsurface (Figure 7d), the satellite-referenced volume transport Q_η is consistent with $Q_{\bar{v}}$, referenced to glider depth-averaged velocity (Figure 11b). The failure of the satellite to capture the strong ESC signal in spring therefore cannot be explained by coarse grid resolution alone. Instead, we suggest that the ESC attains a significant ageostrophic component in spring which, by definition, has no associated surface height gradient, but which is directly observed by glider depth-average velocity measurements. Huthnance et al. (2020) derive an expression for the along-slope velocity field at an idealized eastern boundary, which specifies along-slope baroclinic pressure gradients and along-slope wind forcing as dominant drivers of barotropic flow. Neither of these effects is accounted for when computing $v_\eta(x,\ z)$, whereas $v(x,\ z)$ will incorporate them implicitly. This may go some way toward explaining the discrepancy between $v(x,\ z)$ and $v_\eta(x,\ z)$, particularly in spring. However, evaluating these terms requires additional data and is outside the scope of this work.

4.3. Gliders as Components in Ocean Monitoring Arrays

Transformed and gridded glider Θ observations excellently replicate Θ profiles from the EB1 mooring (Figure 3a). This gives some confidence that glider data transformed in this way can, where appropriate, be used in place of mooring observations and seamlessly integrated into conventional observing arrays. Furthermore, the glider Θ-S profiles offer an improved vertical resolution over moorings, particularly when it comes to resolving surface stratification (Figure 3). This has potential advantages for understanding the dynamics of the shallow summer mixed layer. However, glider S values suffered a bias relative to the calibrated mooring values. Although the effect on the observed circulation was minimal in this study, steps are needed to ensure the accuracy of glider S data before they can replace moorings as the central component in the RT monitoring array. The RT mooring occupation is ongoing, and future mooring data will become available which can be used to calibrate coinciding glider observations. Hence, while extensive glider coverage might potentially reduce the number of moorings required to monitor a given oceanic section, we suggest it is prudent to also deploy at least one moored platform for calibration purposes.

The median time interval between consecutive glider transects was 2.8 days. As a result, the temporal resolution afforded by glider monitoring of the EW is inferior to that of mooring observations (even assuming a continuous glider occupation in EW) and insufficient to resolve synoptic scale variability. The potential for aliasing diurnal and multidiurnal signals means the glider-derived transport time series (Figure 10) is of limited value for studying variability at sub-monthly time scales. However, composites constructed from our 110 glider transects afford new perspectives on the seasonal variability in EW velocity structure (Figure 7) and volume transport (Figure 11b), and continued glider monitoring would better resolve multiannual variability. In summary, gliders are only suitable for monitoring ocean variability over appropriate time scales.

5. Conclusions

We have used 6 years of moored velocity and hydrography observations to elucidate the role and response of the RT to the large-amplitude changes in circulation and hydrography over the wider North Atlantic in the past decade. A pronounced freshening signal indicates that the exceptional freshening event observed in the central SPNA in the mid-2010s (Holliday et al., 2020) impacted the RT around 2017. This coincided with large-amplitude changes in circulation, but we find the two are dynamically unrelated because (a) salinity is not a primary control over the geostrophic circulation and (b) the freshening impacts both sides of the RT so does not greatly alter the dynamic height difference across the RT. Interannual variability in RT circulation is instead driven by temperature changes, with subsurface temperature anomalies at the western boundary playing a primary role.

Glider observations of temperature, salinity, and depth-averaged velocity have improved our understanding of the RT eastern boundary current system in several ways, affording new insights into the spatial structure and seasonal variability of the ESC while also revealing a southward countercurrent over the lower slope. Our results indicate that satellite altimetry is unsuitable for observing narrow boundary currents, and that subsurface velocity observations are required to properly resolve the ESC. The along-isobath transformation developed here allows the glider data to be integrated into a more conventional oceanographic section. Transformed glider hydrography is consistent with corresponding mooring hydrography, but offers an improved vertical resolution and additional horizontal structure. The main limitations of the glider observations are the 1,000 m depth threshold and the large time intervals between successive missions. Continuous glider campaigns using instruments rated below 1,000 m would therefore yield valuable new insights. Regardless, we have demonstrated the potential for gliders as a highly effective tool for observing the currents at the eastern boundary of the RT and, by extension, ocean boundary currents in general.

Data Availability Statement

The mooring and glider data used in this paper can be obtained from https://thredds.sams.ac.uk/thredds/catalog/osnap/catalog.html. GLORYS12V1 reanalysis output was obtained from the Copernicus Marine and Environment Monitoring Service (CMEMS, https://doi.org/10.48670/moi-00021). Satellite-derived absolute dynamic topography data were obtained from CMEMS (https://doi.org/10.48670/moi-00141 and https://doi.org/10.48670/moi-00142). Gridded bathymetry data were obtained General Bathymetric Chart of the Ocean (GEBCO, https://www.gebco.net/data_and_products/historical_data_sets/#gebco_2014).

Acknowledgments
This project was supported by the UK Natural Environment Research Council National Capability programme CLASS NE/R015953/1, NERC Grants UK OSNAP (NE/K010875/1 and NE/K010875/2), UK OSNAP Decade (NE/T00858X/1), and SNAP-DRAGON NE/T013494/1. This project has received funding from the European Union's Horizon 2020 research and innovation programme under grant agreement No. 818123 (iAtlantic). This output reflects only the authors' view and the European Union cannot be held responsible for any use that may be made of the information contained therein. The authors thank Darren Rayner for his work in designing and implementing the mooring array.

References

Barnes, S. L. (1994). Applications of the Barnes objective analysis scheme. Part II: Improving derivative estimates. *Journal of Atmospheric and Oceanic Technology*, *11*(6), 1449–1458. https://doi.org/10.1175/1520-0426(1994)0112.0.co;2

Berx, B., Hansen, B., Østerhus, S., Larsen, K. M., Sherwin, T., & Jochumsen, K. (2013). Combining in situ measurements and altimetry to estimate volume, heat and salt transport variability through the Faroe-Shetland Channel. *Ocean Science*, *9*(4), 639–654. https://doi.org/10.5194/os-9-639-2013

Booth, D. A., & Ellett, D. J. (1983). The Scottish continental slope current. *Continental Shelf Research*, *2*(2–3), 127–146. https://doi.org/10.1016/0278-4343(83)90012-2

Desbruyères, D., Chafik, L., & Maze, G. (2021). A shift in the ocean circulation has warmed the subpolar North Atlantic Ocean since 2016. *Communications Earth and Environment*, *2*(1), 48. https://doi.org/10.1038/s43247-021-00120-y

Dickson, R. R., Gould, W. J., Griffiths, C., Medler, K. J., & Gmitrowicz, E. M. (1986). Seasonality in currents of the Rockall channel. *Proceedings of the Royal Society of Edinburgh, Section B: Biological Sciences*, *88*, https://doi.org/10.1017/s0269727000004498

Ellett, D. J., Edwards, A., & Bowers, R. (1986). The hydrography of the Rockall Channel—An overview. *Proceedings of the Royal Society of Edinburgh, Section B: Biological Sciences*, *88*, 61–81. https://doi.org/10.1017/s0269727000004474

Eriksen, C. C., Osse, T. J., Light, R. D., Wen, T., Lehman, T. W., Sabin, P. L., et al. (2001). Seaglider: A long-range autonomous underwater vehicle for oceanographic research. *IEEE Journal of Oceanic Engineering*, *26*(4), 424–436. https://doi.org/10.1109/48.972073

Fox, A. D., Biastoch, A., Cunningham, S. A., Fraser, N., Handmann, P., Holliday, N. P., et al. (2022). Exceptional freshening and cooling in the eastern subpolar North Atlantic caused by reduced Labrador Sea surface heat loss. *Ocean Science Discussions*, 1–35. https://doi.org/10.5194/os-2022-18

Gary, S. F., Cunningham, S. A., Johnson, C., Houpert, L., Holliday, N. P., Behrens, E., et al. (2018). Seasonal cycles of oceanic transports in the eastern subpolar North Atlantic. *Journal of Geophysical Research: Oceans*, *123*(2), 1471–1484. https://doi.org/10.1002/2017JC013350

Gregor, L., Ryan-Keogh, T. J., Nicholson, S. A., du Plessis, M., Giddy, I., & Swart, S. (2019). Glidertools: A python toolbox for processing underwater glider data. *Frontiers in Marine Science*, *6*. https://doi.org/10.3389/fmars.2019.00738

Holliday, N. P., Bacon, S., Cunningham, S. A., Gary, S. F., Karstensen, J., King, B. A., et al. (2018). Subpolar North Atlantic overturning and gyre-scale circulation in the summers of 2014 and 2016. *Journal of Geophysical Research: Oceans*, *123*(7), 4538–4559. https://doi.org/10.1029/2018JC013841

Holliday, N. P., Bersch, M., Berx, B., Chafik, L., Cunningham, S., Florindo-López, C., et al. (2020). Ocean circulation causes the largest freshening event for 120 years in eastern subpolar North Atlantic. *Nature Communications*, *11*(1), 585. https://doi.org/10.1038/s41467-020-14474-y

Holliday, N. P., Cunningham, S. A., Johnson, C., Gary, S. F., Griffiths, C., Read, J. F., & Sherwin, T. (2015). Multidecadal variability of potential temperature, salinity, and transport in the eastern subpolar North Atlantic. *Journal of Geophysical Research: Oceans*, *120*(9), 5945–5967. https://doi.org/10.1002/2015JC010762

Holliday, N. P., Pollard, R. T., Read, J. F., & Leach, H. (2000). Water mass properties and fluxes in the Rockall Trough, 1975–1998. *Deep Sea Research Part I: Oceanographic Research Papers*, *47*(7), 1303–1332. https://doi.org/10.1016/S0967-0637(99)00109-0

Holliday, P., & Cunningham, S. (2013). The Extended Ellett Line: Discoveries from 65 years of marine observations west of the UK. *Oceanography*, *26*(2). https://doi.org/10.5670/oceanog.2013.17

Houpert, L., Cunningham, S., Fraser, N., Johnson, C., Holliday, N. P., Jones, S., et al. (2020). Observed variability of the North Atlantic Current in the Rockall Trough from 4 years of mooring measurements. *Journal of Geophysical Research: Oceans*, *125*(10), e2020JC016403. https://doi.org/10.1029/2020JC016403

Huthnance, J., Hopkins, J., Berx, B., Dale, A., Holt, J., Hosegood, P., et al. (2022). Ocean shelf exchange, NW European shelf seas: Measurements, estimates and comparisons. *Progress in Oceanography*, *202*, 102760. https://doi.org/10.1016/j.pocean.2022.102760

Huthnance, J. M. (1984). Slope currents and "JEBAR". *Journal of Physical Oceanography*, *14*(4), 795–810. https://doi.org/10.1175/1520-0485(1984)014<0795:sca>2.0.co;2

Huthnance, J. M., & Gould, W. J. (1989). On the northeast Atlantic slope current. https://doi.org/10.1007/978-1-4613-8963-7_7

Huthnance, J. M., Inall, M. E., & Fraser, N. J. (2020). Oceanic density/pressure gradients and slope currents. *Journal of Physical Oceanography*, *50*(6), 1643–1654. https://doi.org/10.1175/JPO-D-19-0134.1

Li, F., Lozier, M. S., Bacon, S., Bower, A. S., Cunningham, S. A., de Jong, M. F., et al. (2021). Subpolar North Atlantic western boundary density anomalies and the meridional overturning circulation. *Nature Communications*, *12*(1), 3002. https://doi.org/10.1038/s41467-021-23350-2

Lozier, M. S., Li, F., Bacon, S., Bahr, F., Bower, A. S., Cunningham, S. A., et al. (2019). A sea change in our view of overturning in the subpolar North Atlantic. *Science*, *363*(6426), 516–521. https://doi.org/10.1126/science.aau6592

Marsh, R., Haigh, I. D., Cunningham, S. A., Inall, M. E., Porter, M., & Moat, B. I. (2017). Large-scale forcing of the European Slope Current and associated inflows to the North Sea. *Ocean Science*, *13*(2), 315–335. https://doi.org/10.5194/os-13-315-2017

Moritz, M., Jochumsen, K., Kieke, D., Klein, B., Klein, H., Köllner, M., & Rhein, M. (2021). Volume transport time series and variability of the North Atlantic eastern boundary current at Goban Spur. *Journal of Geophysical Research: Oceans*, *126*(9), e2021JC017393. https://doi.org/10.1029/2021JC017393

SCOR, I. (2010). IAPSO: The international thermodynamic equation of seawater–2010: Calculation and use of thermodynamic properties, intergovernmental oceanographic commission, manuals and guides no. 56. *UNESCO, Manuals and Guides*, *56*.

Souza, A. J., Simpson, J. H., Harikrishnan, M., & Malarkey, J. (2001). Flow structure and seasonality in the Hebridean Slope Current. *Oceanologica Acta*, *24*, 63–76. https://doi.org/10.1016/s0399-1784(00)01103-8

Xu, W., Miller, P. I., Quartly, G. D., & Pingree, R. D. (2015). Seasonality and interannual variability of the European Slope Current from 20 years of altimeter data compared with in situ measurements. *Remote Sensing of Environment*, *162*, 196–207. https://doi.org/10.1016/j.rse.2015.02.008